Point Spread Function And Spatial Resolution Analysis Of Multi-Focus Plenoptic Cameras

P. Schleuniger[1,*], M. Brunel[1], J.-B. Blaisot[1]

1: UMR 6614 CORIA, Université de Rouen, France
*Corresponding author: schleunp@coria.fr

Keywords: Light field imaging, Point spread function, 3D measurements.

ABSTRACT

With the recent development of plenoptic cameras, light field imaging has become a reliable solution for 3D metrology. Plenoptic cameras allow to recover the 3D information of a scene with a single acquisition and only one camera. These advantages make light field imaging particularly interesting for the metrology of two-phase flows. The measurement depth of a back-light imaging set-up can be determined by the calibration of the Point Spread Function (PSF) of the optical system. This study provides a method, adapted to multi-focus plenoptic cameras, to measure the PSF width from reconstructed images. We used a calibration target composed of multiple calibrated opaque disks and a diffuse backlight illumination set-up. The PSF width is estimated by measuring the grayscale gradient at the interface of the images of the disks. Coupled with the depth information provided by the plenoptic camera, we obtained the evolution of the PSF at different depth planes. The information on the PSF enables to obtain the focus criterion which sets the limits of the measurement volume. The spatial resolution of the reconstructed images is obtained from the PSF. The results obtained for the resolution as a function of virtual depth are consistent with results from previous studies.

1. Introduction

Having access to the third dimension for particle diagnostics in flows is eagerly anticipated among researchers. Most of the phenomena encountered in fluid mechanics are tridimensional by nature such as liquid atomisation, bubbly flows or the movement of seeding particles in a turbulent flow. Several imaging techniques have been used to obtain the 3D position and size of particles in flows such as holography (Wu et al., 2021; Gao et al., 2013), interferometric particle imaging (Shen et al., 2013) or stereo vision (El-Adawy et al., 2021; Chang et al., 2023). However, those techniques have several drawbacks. On one hand, hologram processing requires considerable computing time (Onofri & Lamadie, 2022) and parasitic fringes caused by the phase reconstruction can appear (Onofri, 2023) and make image analysis more challenging, especially for dense two-phase flows. On the other hand, multi-camera systems can be used with regular diffuse background illuminated

set-ups, but the resulting installation can be bulky and the 3D calibration of all the cameras may be challenging (Masuk et al., 2019). Recent developments of plenoptic imaging in the field of flow metrology have been reported (Chen et al., 2023; Fahringer & Thurow, 2012; Fahringer et al., 2015; Fahringer & Thurow, 2018) which has the advantage of not relying on a coherent light source nor multiple cameras. A plenoptic camera can be used to perform light field sampling, allowing depth estimation of a scene with a single shot. Another key feature of those cameras is to be able to perform post acquisition refocusing like in holography. Plenoptic cameras are also able to reconstruct images that display all elements in the scene as focused. Coupled with the corresponding depth map, we can obtain the 3D position of particles as well as size distribution within the sampling volume (Hall et al., 2019). If we want to perform particle size measurement with these reconstructed images, it is then mandatory to know the point spread function (PSF) of the reconstructed images. The PSF is a fundamental property of an optical system describing the image of an object point onto the sensor. For traditional image capturing system, the PSF can provide the focus criterion as shown in (Blaisot, 2012) and allows to define the limit of the measurement volume for a given minimum size of particle. If this parameter is not taken into account, the resulting size distribution may be biased. Previous works tackled the PSF estimation of plenoptic cameras by modelling the PSF of a main lens and a single microlens (Jin et al., 2017) or by experimentally measuring the PSF of each micro image along the raw image (Eberhart et al., 2021). In this work, we focus on the PSF estimation of the reconstructed all-in-focus images as those images are the ones which will be processed to obtain the 3D position and size of the particles. We will also study the resolution of the multi-focus camera deduced from the study of the PSF.

2. Light field imaging principle

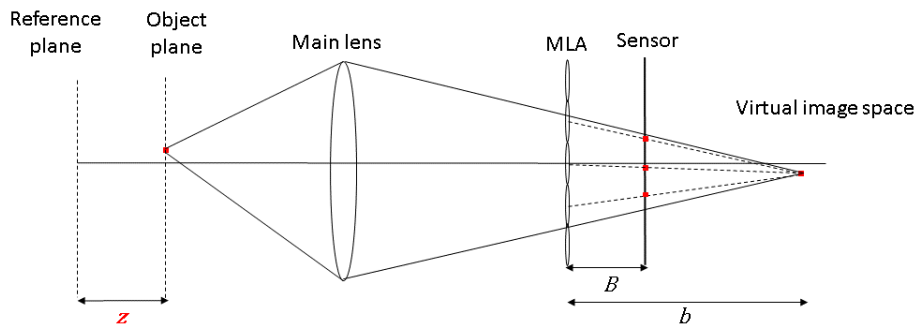### 2.1. Image formation and depth estimation

Figure 1. Imaging principle of the plenoptic camera

Plenoptic cameras differ from traditional cameras by the addition of an array composed of multiple microscopic lenses between the main lens and the sensor. The role of this microlens array (MLA) is to sample both the positional and directional information of incoming light rays. Each microlens will act as a micro camera and project a portion of the virtual image formed by the main lens onto the sensor as shown in Fig. 1. Most advanced plenoptic cameras have an MLA composed of three different types of lenses, each type having its own focal length. Those are called multi-focus plenoptic cameras (MFPC) and they provide a larger depth of field at the cost of a lower spatial resolution (Perwass & Wietzke, 2012). The camera used in this study is a MFPC.

The first step for depth estimation is to compute the disparity between neighbouring micro images as described in Fig. 2. From the disparity, we can obtain the virtual depth with the following relation :

$$v = \frac{b}{B} \tag{1}$$

with b being the distance between the virtual image plane and the MLA plane and B the distance between the MLA and the sensor (see Fig. 1). For this study, we will use the virtual depth as this quantity is dimensionless and thus allows to compare different MFPCs whatever the distance B. Moreover, the virtual depth is an intuitive quantity as it represents the number of microlenses along an epipolar line that actually see the object point and thus, is directly linked to the angular resolution of the MFPC. A crop of a raw image representing an opaque disk at a virtual depth $v = 3$ is shown in Fig. 3a. We can clearly see the redundancy of the disk image among neighbouring micro-images.

Thanks to the redundancy appearing on the sensor, we can perform a virtual depth estimation. We will first use the principle of stereo matching in order to compute the disparity d with sub-pixel accuracy between neighbouring micro-images. An example of two micro-images whose centers are separated by the distance D is shown on Fig. 2. If the disparity of a feature (represented by red square on Fig. 2) appearing on both micro-images is d, then the virtual depth of this feature is obtained with the relation:

$$v = \frac{D}{d} \tag{2}$$

Knowing the virtual depth v and with a proper 3D calibration, we can obtain the 3D position in the object space and a metric depth map can be estimated (Zeller et al., 2014; Heinze et al., 2016).
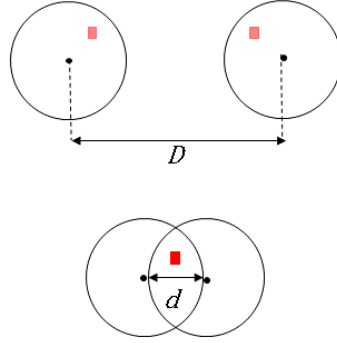
Figure 2. Disparity estimation between two neighbouring micro-images

(a)   (b)

Figure 3. (a) Crop of a raw light field image of a calibration target, (b) Rendered all-focused image of the target

2.2. All-focused image reconstruction

One of the key features of the plenoptic camera is its ability to perform refocusing after capturing a scene. It is also possible to reconstruct an image where all the elements of the scene within the depth of field of the camera appear as focused. This image can be rendered by sampling a patch of pixels from each micro image. The size of the patch that needs to be sampled is directly linked to the depth location of the feature appearing on the micro-image, thus it is linked to the virtual depth. Tiling all the patches depending on the position of their respective micro image on the sensor will result in a new image similar to the one obtained with a regular camera. This image is called "all-focused" image that can then be processed with regular image analysis tools. A crop of a raw image and its corresponding all-focused image are shown in Fig. 3a and Fig. 3b respectively.

Although it is possible to obtain an all-focused image without knowing the virtual depth associated to each microlens (Wanner et al., 2011), having information about v makes the processing more straightforward.

3. Experimental measurements

3.1. Experimental set-up

Our MFPC plenoptic camera model is a Raytrix R29. It is equipped with a 100 mm f/2.8 macro lens and has a 6576*4384 pixels sensor. The pixel size is 5.5 µm. In our configuration, the camera lens behaves like a telecentric lens which implies a constant magnification over the whole depth of field and avoids perspective effects. We use a transparent calibration target with 125 µm calibrated opaque disks that we attach on a mirror mount. The mount is placed on a micrometric translation platform. We can adjust the orientation of the target thanks to the mirror mount. The back of the calibration target is illuminated by a diffuse white light source. We place the target at the farthest plane from the camera where virtual depth estimation can still be performed, and we orient the target in order to have the most uniform virtual depth map on the RxLive software. The farthest plane will be the reference plane at the depth $z = 0$ mm. For each target location distant by 50 µm along the optical axis, the light field is captured, and both the virtual depth as well as the all-focused image are computed. The resolution of both the all-focused image and the corresponding depth map is 3288*2192 pixels which is one quarter of the full sensor resolution. The magnification at depth $z = 0$ mm is 175.67 pixel/mm on the all-focused images. The depth of field of the plenoptic camera is measured at the nearest location $z = 4.5$ mm.

3.2. Point Spread function measurement

In order to estimate the measurement volume and also the size of the smallest measurable particle, we need to perform the calibration of the PSF. The technique used is the one proposed by Blaisot (2012) and rely on the measurement of the grayscale gradient at the interface on images of calibrated opaque disks.

Based on Fourier optics, the illumination distribution on the image plane $i(x, y)$ can be modelled as the convolution product of the irradiance distribution of the object plane $o(x, y)$ and the PSF :

$$i(x, y) = o(x, y) \otimes PSF(x, y) \tag{3}$$

In the case of a polychromatic light source, the PSF shape can be represented by a Gaussian function as proposed by Pentland (1987) :

$$PSF(r) = \frac{2}{\pi \chi^2} e^{\frac{-2r^2}{\chi^2}} \tag{4}$$

Where χ is the half width of the PSF. The value χ is linked to the sharpness of the image as its value is minimum at the focus plane and increases as the image is formed away from the focus plane. χ is then linked to the grayscale gradient at the border of the object. χ is obtained with the relation :

$$\chi = \sqrt{2}\,\frac{\tilde{g}_{0.50}}{g_{0.50}} \tag{5}$$

where $g_{0.50}$ is the measured grayscale gradient on the normalised image in $pixel^{-1}$ at a relative grayscale level of 50 %. $\tilde{g}_{0.50}$ is a dimensionless grayscale gradient which depends on the normalised contrast of the image. The dimensionless grayscale gradient is obtained with the method depicted in Fig. 4. The shape of the intensity profile depends on the dimensionless size of the object : bigger objects tend to have a U-shape whereas smaller object's profile is closer to a V-shape as the profile shown in the Fig. 4.
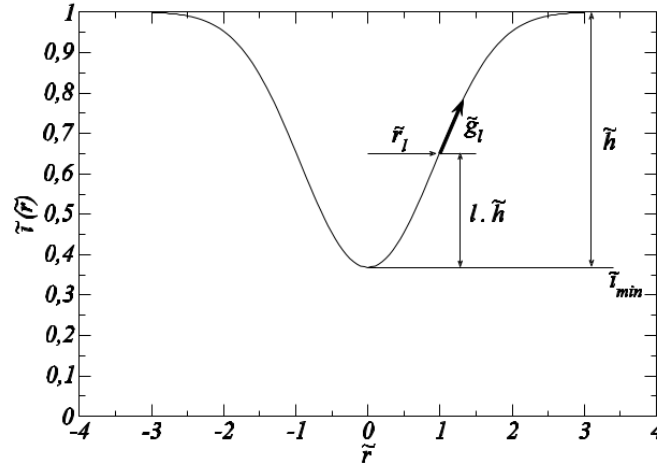

Figure 4. Normalised illumination radial profile $\tilde{i}$ as a function of the normalised radial coordinate $\tilde{r}$. The relation between the normalised radial coordinate and radial coordinate r is : $\tilde{r} = \sqrt{2}\,r/\chi$. The dimensionless grayscale gradient $\tilde{g}_l$ is measured at a relative level l. Image taken from Blaisot (2012).

The PSF width 2χ for a given depth plane is obtained by averaging all the PSF width measured at each black disks of the calibration target. For each depth plane, the average is performed on more than 3700 disks. The variation of the PSF width is shown in Fig. 5a as a function of the virtual depth or in Fig. 5b as a function of the location of the calibration target. We notice that the PSF behaviour is different from classical image acquisition systems. For standard cameras, the PSF has a V-shape and reaches its minimum value where the focus plane is located (Fdida & Blaisot, 2009). Here, the PSF increases as the virtual depth increases. We also notice a steep increase of the PSF width around $v = 3$ and $v = 4$. As shown in Fig. 5a, those zones correspond to transitions between two microlens depth domains. Theses microlens domains correspond to the respective depth of field of a single type of microlens. As mentioned before, the MLA is composed of 3 different microlenses with different focal lengths. As the calibration target is perpendicular to the optical axis, the reconstruction of the all-focused image is equivalent to a refocusing reconstruction because all the objects are located in the same depth plane. As a result, each all-focused image is rendered using only one type of microlens, the type being chosen based on the previously estimated virtual depth (see Eq. 2)

With the information about the PSF width along the whole depth of field, we need to set the focus criterion χ_{max} that will determine the limit of the measurement volume. The value of χ_{max} depends on the minimum contrast C_{min} and the size of the smallest significant object appearing on the all-focused image. The minimum contrast C_{min} is set to 0.1. It corresponds to the contrast threshold of an image below which an object won't be sizable. The minimum size is fixed by the minimum number of pixels required to constitute an object $N = 6$. The focus criterion χ_{max} is given by Eq. 6:

$$\chi_{max} = \frac{\sqrt{2}}{\tilde{a}} p_o \sqrt{\frac{N}{\pi}} \tag{6}$$

with p_o the physical size of a pixel in the object space and $\tilde{a}$, the dimensionless object radius corresponding to a contrast C_{min}. $\tilde{a}$ is set to 0.45 (see Blaisot (2012)).

The resulting value for the focus criterion is then $2\chi_{max} = 49$ µm. Looking at Fig. 5a, this implies that the measurement volume in the virtual image space is within the range $v = 2.86$ and $v = 5.7$. Looking at Fig. 5b, the resulting depth of the measurement volume in object space is then 1.75 mm which is around one third of the total depth of field of the MFPC.
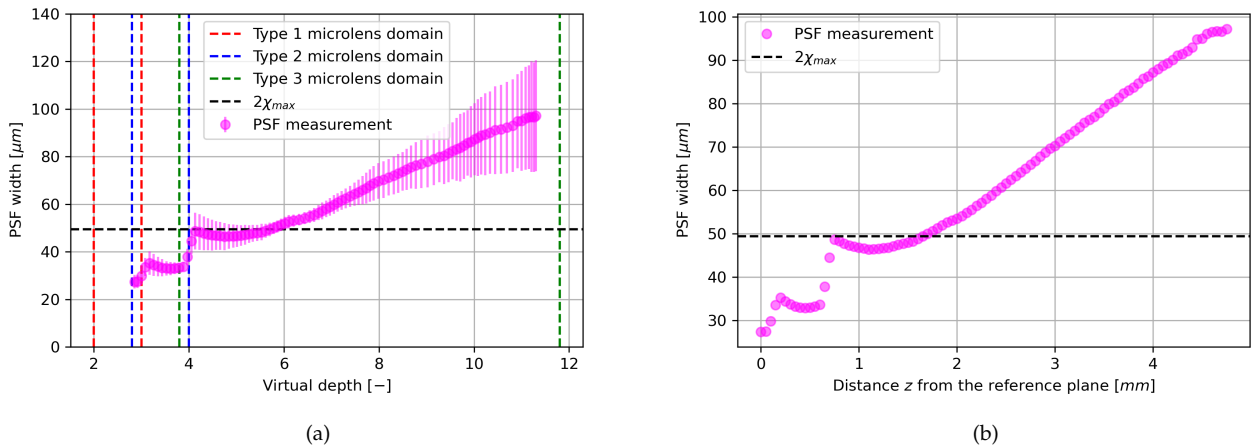

Figure 5. (a) Evolution of the PSF width with the virtual depth v, (b) Evolution of the PSF width with the depth position z in the object space

In traditional imaging systems used for granulometry, the aperture of the lens can be reduced in order to extend the depth of field at the cost of a lower contrast. However, this solution is not viable for plenoptic cameras as the working f-number of both the main lens and the microlenses must be matched. Reducing the aperture of the main lens will result in smaller micro images, thus reducing the spatial resolution with fewer pixels per micro-image. Moreover, it will reduce the depth of field because the minimum value of the virtual depth will increase due to a lower microlens diameter.

3.3. Effective resolution ratio analysis

Another parameter we can extract from the reconstructed images is the effective resolution ratio. This quantity is a dimensionless resolution representing the ratio between the actual resolution of the image over the maximum achievable resolution of the sensor. Thanks to the previous study of the PSF, we can derive the effective resolution ratio from the MTF50 method. First, we need to compute the Modulation Transfer Function (MTF) of the system which is simply the 2D Fourier Transform of the PSF.

After a 2D Fourier transform of equation Eq. 4, the resulting MTF is :

$$MTF(\rho) = e^{\frac{-\pi^2 \chi^2}{2} \rho^2} \tag{7}$$

with ρ being the spatial frequency. Note that the value used for χ is the value in the image space.

From the MTF we can obtain the frequency associated to the MTF value at a 50 % relative level which implies calculating the half width at half height of this Gaussian-like function :

$$f_{50} = \frac{\sqrt{2\ln(2)}}{\pi\chi} \tag{8}$$

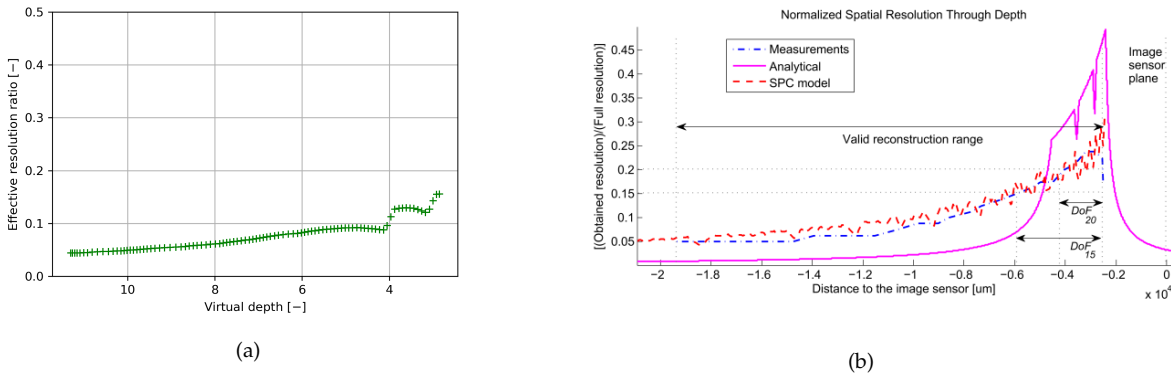This frequency is normalised by the cutoff frequency of the sensor which is 0.5 cycles/pixel.

Figure 6. (a) Evolution of effective resolution ratio with the virtual depth v, (b) Evolution of the effective resolution ratio with the distance between the sensor and the virtual image (from Damghanian et al. (2014). The equivalent virtual depth v can be obtained by dividing the distance to the image sensor by the MLA-sensor distance being 2.5 mm in this case and adding 1 to the result.)

The evolution of the effective resolution ratio depending on the virtual depth is presented in Fig. 6a. It is also compared to the theoretical model, the Sampling Pattern Cube (SPC) model as well

as experimental results from Damghanian et al. (2014) in Fig. 6b. Overall, our experimental results show a good agreement with Damghanian's results. However, we notice two steep decreases of resolution for $v = 3$ and $v = 4$. This is the consequence of the important increase of the PSF width shown above. The analytical model in Fig. 6b was developed by Perwass & Wietzke (2012). Looking at the analytical model, important loss of resolution can occur during the transition from a microlens depth of field to another type of microlens depth of field. Note that the domain of depth estimation starts at $v = 3$ in our case even though the minimum value required for stereo matching is $v = 2$. This is due to coma appearing on the border of the micro images. In order to avoid this effect that might have an impact on the disparity estimation, we chose to reduce the effective diameter of the micro images by not using the pixels from the outer border of the micro images on a 3 pixels wide border. This results in a higher minimum virtual depth. The fact that the effective resolution ratio decreases as the virtual depth increases is consistent. As mentioned before, the virtual depth is linked to the number of redundancy of an image point on the raw image in one direction which means that v represents the angular resolution of the MFPC for a given object plane. The more redundancies, the more pixels are used to replicate one image point and thus, less different image points can be represented which leads to a lower spatial resolution.

4. Conclusions

We proposed a PSF calibration method adapted to multi-focus plenoptic cameras (MFPCs) in order to determine the focus criterion and establish the limit of the measurement volume for 3D particle location and size measurement. Thanks to previous work for regular imaging system, we saw that for MFPC, the PSF width increases as the object is located closer to the camera. As a result, it limits the measurement depth range to one third of the actual depth of field of the MFPC. We also managed to deduce the evolution of the effective resolution ratio from the PSF width and the results are similar to those obtained from other studies. We also stressed the trade-off between the angular and the spatial resolution induced by the MFPC as the higher the angular resolution, the higher the PSF width and thus, the lower the spatial resolution.

Acknowledgements

Nomenclature

$\tilde{a}$ Dimensionless object radius [m]

b	MLA-virtual image distance [m]
B	MLA-sensor distance [m]
C_{min}	Minimum contrast [-]
d	Disparity [m]
D	Distance between two micro-images [m]
f_{50}	Spatial frequency associated to the MTF at a 50% relative level [m^{-1}]
$\tilde{g}_{0.50}$	Dimensionless grayscale gradient [-]
$g_{0.50}$	Grayscale gradient [m^{-1}]
MTF	Modulation Transfer Function [-]
$MTF50$	Modulation Transfer Function value at a 50% relative level [-]
N	Number of pixels [-]
p_o	Physical size of a pixel [m]
PSF	Point Spread Function [m^{-2}]
r	Radial coordinate [m]
$\tilde{r}$	Normalised radial coordinate [-]
v	Virtual depth [-]
z	Distance from the reference plane [m]
χ	PSF half width [m]
χ_{max}	PSF half width for the focus criterion [m]

References

Blaisot, J.-B. (2012, September). Drop size and drop size distribution measurements by image analysis. In *International conference on liquid atomization and spray systems.*

Chang, Y., Müller, C., Kováts, P., Guo, L., & Zähringer, K. (2023, December). Hydrodynamics and shape reconstruction of single rising air bubbles in water using high-speed tomographic particle tracking velocimetry and 3d geometric reconstruction. *Experiments in Fluids*, *65*(1). doi: 10.1007/s00348-023-03746-0

Chen, L., Xu, C., Li, J., & Zhang, B. (2023, January). A 3d measurement method of bubbles based on edge gradient segmentation of light field images. *Chemical Engineering Journal*, *452*, 139590. doi: 10.1016/j.cej.2022.139590

Damghanian, M., Olsson, R., Sjostrom, M., Erdmann, A., & Perwass, C. (2014, October). Spatial resolution in a multi-focus plenoptic camera. In *2014 ieee international conference on image processing (icip).* IEEE. doi: 10.1109/icip.2014.7025387

Eberhart, M., Loehle, S., & Offenhäuser, P. (2021, July). 3-d visualization of transparent fluid flows from snapshot light field data. *Experiments in Fluids*, *62*(8). doi: 10.1007/s00348-021-03255-y

El-Adawy, M., Heikal, M. R., Aziz, A. R. A., & Adewale Opatola, R. (2021, June). Stereoscopic particle image velocimetry for engine flow measurements: Principles and applications. *Alexandria Engineering Journal*, *60*(3), 3327–3344. doi: 10.1016/j.aej.2021.01.060

Fahringer, T. W., Lynch, K. P., & Thurow, B. S. (2015, September). Volumetric particle image velocimetry with a single plenoptic camera. *Measurement Science and Technology*, *26*(11), 115201. doi: 10.1088/0957-0233/26/11/115201

Fahringer, T. W., & Thurow, B. (2012, June). Tomographic reconstruction of a 3-d flow field using a plenoptic camera. In *42nd aiaa fluid dynamics conference and exhibit.* American Institute of Aeronautics and Astronautics. doi: 10.2514/6.2012-2826

Fahringer, T. W., & Thurow, B. S. (2018, May). Plenoptic particle image velocimetry with multiple plenoptic cameras. *Measurement Science and Technology*, *29*(7), 075202. doi: 10.1088/1361-6501/aabe1d

Fdida, N., & Blaisot, J.-B. (2009, December). Drop size distribution measured by imaging: determination of the measurement volume by the calibration of the point spread function. *Measurement Science and Technology*, *21*(2), 025501. doi: 10.1088/0957-0233/21/2/025501

Gao, J., Guildenbecher, D. R., Reu, P. L., Kulkarni, V., Sojka, P. E., & Chen, J. (2013, May). Quantitative, three-dimensional diagnostics of multiphase drop fragmentation via digital in-line holography. *Optics Letters*, *38*(11), 1893. doi: 10.1364/ol.38.001893

Hall, E. M., Guildenbecher, D. R., & Thurow, B. S. (2019, January). Refinement and application of 3d particle location from perspective shifted plenoptic images. In *Aiaa scitech 2019 forum.* American Institute of Aeronautics and Astronautics. doi: 10.2514/6.2019-0268

Heinze, C., Spyropoulos, S., Hussmann, S., & Perwass, C. (2016). Automated robust metric calibration algorithm for 3d camera system. *IEEE Transactions on Instrumentation and Measurement*, *65*(5), 1197–1205.

Jin, X., Liu, L., Chen, Y., & Dai, Q. (2017, April). Point spread function and depth-invariant focal sweep point spread function for plenoptic camera 20. *Optics Express*, *25*(9), 9947. doi: 10.1364/oe.25.009947

Masuk, A. U. M., Salibindla, A., & Ni, R. (2019, November). A robust virtual-camera 3d shape reconstruction of deforming bubbles/droplets with additional physical constraints. *International Journal of Multiphase Flow*, *120*, 103088. doi: 10.1016/j.ijmultiphaseflow.2019.103088

Onofri, F. R. A. (2023, February). Granulométrie optique des écoulements. *Mesures physiques*. doi: 10.51257/a-v1-r2165

Onofri, F. R. A., & Lamadie, F. (2022, July). Digital in-line holography and the photonic jet method: routines and graphical user interfaces to generate numerical standards with the lorenz-mie theory. In I. S. TÉCNICO (Ed.), *International symposium on applications of laser and imaging techniques to fluid mechanics (lxlaser2022)* (p. Holography 3). Lisbonne, Portugal. Retrieved from `https://hal.science/hal-03808011`

Pentland, A. P. (1987, July). A new sense for depth of field. *IEEE Transactions on Pattern Analysis and Machine Intelligence*, *PAMI-9*(4), 523–531. doi: 10.1109/tpami.1987.4767940

Perwass, C., & Wietzke, L. (2012). Single lens 3d-camera with extended depth-of-field. In *Human vision and electronic imaging xvii* (Vol. 8291, p. 829108).

Shen, H., Coetmellec, S., & Brunel, M. (2013). Simultaneous 3d location and size measurement of spherical bubbles using cylindrical interferometric out-of-focus imaging. *Journal of Quantitative Spectroscopy and Radiative Transfer*, *131*, 153-159. Retrieved from `https://www.sciencedirect.com/science/article/pii/S0022407313001441` (Concepts in electromagnetic scattering for particulate-systems characterization) doi: https://doi.org/10.1016/j.jqsrt.2013.04.009

Wanner, S., Fehr, J., & Jähne, B. (2011). Generating epi representations of 4d light fields with a single lens focused plenoptic camera. In *International symposium on visual computing* (pp. 90–101).

Wu, Y., Wang, L., Lin, W., Song, G., He, Y., Wu, X., . . . Cen, K. (2021, January). Picosecond pulsed digital off-axis holography for near-nozzle droplet size and 3d distribution measurement of a swirl kerosene spray. *Fuel*, *283*, 119124. doi: 10.1016/j.fuel.2020.119124

Zeller, N., Quint, F., & Stilla, U. (2014, August). Calibration and accuracy analysis of a focused plenoptic camera. *ISPRS Annals of the Photogrammetry, Remote Sensing and Spatial Information Sciences*, *II–3*, 205–212. doi: 10.5194/isprsannals-ii-3-205-2014